ADVANCED FUNCTIONAL MATERIALS
www.afm-journal.de

Diamond-Based Supercapacitors with Ultrahigh Cyclic Stability Through Dual-Phase MnO_2-Graphitic Transformation Induced by High-Dose Mn-Ion Implantation

Sujit Deshmukh, Srinivasu Kunuku, Pawel Jakobczyk, Adrian Olejnik, Chien-Hsu Chen, Huan Niu, Bing Yang, Nianjun Yang,* and Robert Bogdanowicz**

While occasionally being able to charge and discharge more quickly than batteries, carbon-based electrochemical supercapacitors (SCs) are nevertheless limited by their simplicity of processing, adjustable porosity, and lack of electrocatalytic active sites for a range of redox reactions. Even SCs based on the most stable form of carbon (sp^3 carbon/diamond) have a poor energy density and inadequate capacitance retention during long charge/discharge cycles, limiting their practical applications. To construct a SC with improved cycling stability/energy density Mn-ion implanted (high-dose; 10^{15}–10^{17} ions cm^{-2}) boron doped diamond (Mn-BDD) films have been prepared. Mn ion implantation and post-annealing process results in an in situ graphitization (sp^2 phase) and growth of MnO_2 phase with roundish granular grains on the BDD film, which is favorable for ion transport. The dual advantage of both sp^2 (graphitic phase) and sp^3 (diamond phase) carbons with an additional pseudocapacitor (MnO_2) component provides a unique and critical function in achieving high-energy SC performance. The capacitance of Mn-BDD electrode in a redox active aqueous electrolyte (0.05 M $Fe(CN)_6^{3-/4-}$ + 1 M Na_2SO_4) is as high as 51 mF cm^{-2} at 10 mV s^{-1} with exceptional cyclic stability (≈100% capacitance even after 10 000 charge/discharge cycles) placing it among the best-performing SCs. Furthermore, the ultrahigh capacitance retention (≈80% retention after 88 000 charge/discharge cycles) in a gel electrolyte containing a two-electrode configuration shows a promising prospect for high-rate electrochemical capacitive energy storage applications.

1. Introduction

The growing demand for energy generation and storage in electronic gadgets, electric cars, and other applications emphasizes the need for high-capacity/energy-storage devices.[1,2] Supercapacitors (SCs) also known as ultracapacitors, or electrochemical (EC) capacitors are the emerging class of energy storage devices that stored energy in the form of electrical double-layer capacitor (accumulation of charge across the electrode-electrolyte interface) or pseudocapactor (charge transfer across the electrode-electrolyte interface). As compared to batteries, SCs have higher power densities, quicker charging-discharging cycles with longer lifetimes, a wider range of working temperatures, and improved safety.[3] To attain a high capacitance from SCs, the electrode material must be electrically conductive, electrochemically stable, and have a large specific surface area. In this context, sp^2 carbon-based material with diverse dimensionality (ranging from 0 to 3D), shapes, and size distribution have been dominating over the last two decades due to its widespread availability and large

S. Deshmukh, S. Kunuku, P. Jakobczyk, A. Olejnik, R. Bogdanowicz
Department of Metrology and Optoelectronics
Faculty of Electronics
Telecommunications
and Informatics
Gdansk University of Technology
11/12 G. Narutowicza Str., 80-233 Gdansk, Poland
E-mail: sujit.deshmukh@pg.edu.pl; rbogdan@eti.pg.edu.pl

The ORCID identification number(s) for the author(s) of this article can be found under https://doi.org/10.1002/adfm.202308617

DOI: 10.1002/adfm.202308617

C.-H. Chen, H. Niu
Accelerator Laboratory
Nuclear Science and Technology Development Center
National Tsing Hua University
Hsinchu 300044, Taiwan

B. Yang
Shenyang National Laboratory for Materials Science
Institute of Metal Research (IMR)
Chinese Academy of Sciences (CAS)
No. 72 Wenhua Road, Shenyang 110016, China

N. Yang
Department of Chemistry
Hasselt University
Agoralaan-Gebouw F, 3590 Diepenbeek, Belgium
E-mail: nianjun.yang@uhasselt.be

N. Yang
Institute of Materials Research
Hasselt University
Wetenschapspark 1, 3590 Diepenbeek, Belgium

specific capacitance.[4,5] However small overpotential for oxygen and hydrogen evolution reaction in aqueous solution reduces the working potential window of such SCs within ≈1.23 V which limits the energy storage performance significantly.[2,6] Therefore, in order to develop a stable SC, the synthesis of proper electrode materials is thus highly demanded.

Boron doped diamond (BDD) is a promising sp^3 carbon material to construct electrical double-layer capacitors (EDLCs).[7] Apart from its general advantages, such as chemical inertness/stability, and high thermal conductivity, it has unique EC features, such as a large potential window in both aqueous and organic electrolytes, resulting in high energy and power density SCs. For example, K. Honda et al. showed 1st time to construct EDLC using nanoporous honeycomb diamond electrodes in both aqueous and organic electrolytes.[8] The working potential window was 2.5 V and 7.3 V in aqueous and organic electrolytes respectively, which is substantially greater than that of sp^2 carbon electrodes such as activated carbon, glassy carbon, graphite, etc.[8–10] However, the low surface area of a conventional planar BDD restricts its application in the realm of energy storage.[11] To improve the capacitance of BDD the alternative approach is to combine BDD with a pseudocapacitive material or enlarge the surface area by creating micro/nanostructures on BDD.[12–15]

Manganese oxides (MnO_x) is a long-standing material of interest for EC energy storage which involves both double-layer charging and change in Mn redox state corresponding to pseudocapacitance.[16,17] MnO_x has a long history as an electrode material for energy storage devices due to its low cost and non-toxicity.[16] The theoretical specific capacitance of MnO_2 is ≈1370 F $g_{MnO2}{}^{-1}$ based on one-electron transfer redox reaction, although this high value can only be attained practically for ultrathin MnO_2 film or nanosized particles.[18] Another key weakness of this transition metal oxide is its limited electrical conductivity. To effectively utilize the MnO_x material, one interesting approach is the integration of nanosized MnO_x with conductive carbon framework. The use of MnO_x in combination with several types of carbons, such as carbon nanotubes, activated carbon, and conductive diamond, resulted in a considerable performance improvement.[19–21] The reported enhancement, however, is only evident for a small amount of metal loading on the carbon electrode since the high mass loading of MnO_x significantly reduces the material's theoretical advantage and eventually yields a relatively low specific capacitance value.[22] Therefore, limited loading of MnO_x on carbon framework remains a major challenge.

Ion implantation is a powerful and efficient technique that has been used for controlled doping of transition metal ions into the diamond lattice to modulate their electrical characteristics. Metal ion irradiation not only creates different color center defects on diamond lattice but also breaks the C-C (sp^3) bond to form additional sp^2 bonded carbons.[23,24] This facilitates an additional electrical conduction pathway across the interconnected grain boundary of diamond lattice. Additionally, high-energy metal ion irradiation creates nano/microstructures or pores on the diamond surface which can improve the electrolyte contacts in the ion-accessible surface area of SCs.[24] Furthermore, Mn ion-implanted diamond with post-annealing treatment can create graphitized carbon at the diamond grain boundaries and could be a promising approach to prepare a high-performance SC electrode.

In the present work, the combined effect of Mn ion implantation on microwave plasma enhanced chemical vapor deposition (MWPECVD) grown BDD surface and subsequent post-annealing effect on their EC SC performance was investigated. Here Mn ion implanted BDD (Mn-BDD) films were prepared by high dose (10^{15}–10^{17} ions cm^{-2}) Mn ion implantation into MWPECVD-grown BDD films. The post-annealing treatment resulted in a significantly different granular BDD surface (as described in SEM image analysis) consisting of graphitized carbon at the diamond grain boundaries and the appearance of the MnO_2 phase (confirmed through XPS analysis), both of which are beneficial for capacitive energy storage.[22,24] The prepared electrodes were used as an SC in aqueous electrolyte, redox species contained aqueous electrolyte and solid-state gel electrolytes as well. The synergistic combination of MnO_2, exceptional EC stability of diamond lattice, and controlled growth of nanographitic phase at diamond grain boundaries resulted in a high specific capacitance of 51 mF cm^{-2} at 10 mV s^{-1} (redox active aqueous electrolyte) and provided ultra-high cyclic stability (80% retention after 88 000 cycles) in two-electrode configuration, making the electrode very promising for EC energy storage application.

2. Results and Discussion

2.1. Characterization of Mn Ion-Implanted Boron Doped Diamond Films

The schematic diagram of **Figure 1**a represents a BDD film prepared on Si substrate (experimental details are given in supporting information), Mn ion implantation on the BDD film (Mn-BDD), and post-annealed treatment (Mn-BDD_{AN}) to transform the surface to granular structure. Scanning electron microscopy (SEM) analysis of the BDD thin film's surface morphology (Figure 1b) revealed faceted grains with a size range of 300–500 nm (Thickness of the film ≈600 nm) due to high B doping concentrations B/C ≈10 000 ppm.[25] The uneven grain sizes of BDD thin films are due to the secondary nucleation caused by high boron doping concentration.[26,27] The impact of high-dose Mn ion implantation (10^{15}–10^{17} ions cm^{-2}) was observed by analyzing the surface morphology of as-implanted Mn-BDD thin films (Figure 1c). The sharp edges of faceted grains of Mn-BDD thin films were diminished by the bombardment of the implanted Mn ions. The penetration depth (d_p) was estimated using Stopping and Range of Ions in Matter simulations. Figure S1 (supporting information file) depicts the Mn-ion distribution at an implantation energy of 200 keV and the d_p value of 90 nm with straggle of 21 nm. The impact of implanted Mn ions causes damage to surface morphology, crystalline nature, and bonding characteristics of BDD thin films.[24] The high dose ion implantation is similar to thin film deposition because all the implanted ions might not be inserted into diamond films/diamond lattice, as a result, a fraction of implanted Mn ions would be placed on the surface of BDD thin films.[24,28] The post-annealing process has instigated a significant change in the surface morphology and bonding characteristics of Mn-BDD thin films. First, the faceted BDD grains were transformed to irregularly shaped small grains of 50–100 nm size and the continuous Mn-BDD thin film has been converted to a porous structured material (Figure 1d).

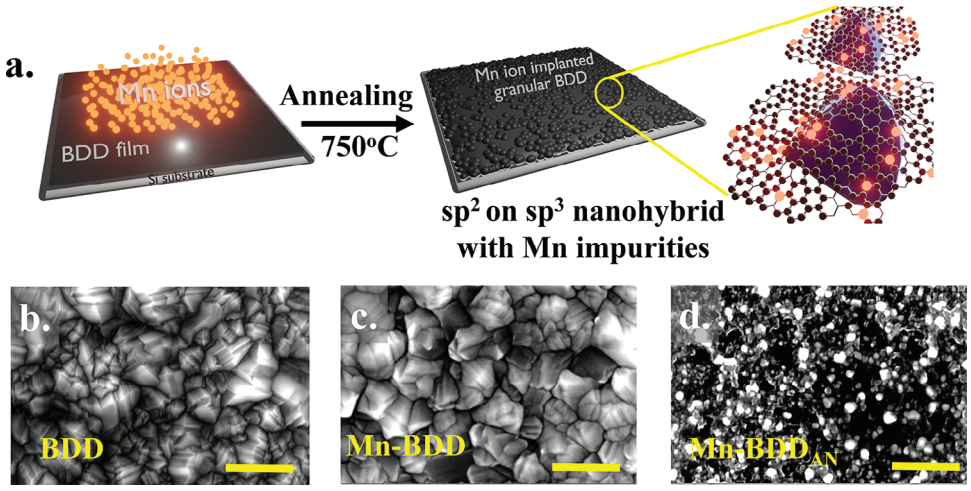

Figure 1. a) Schematic diagram of the formation of graphitic carbon with Mn impurities on the diamond surface during the production of granular Mn ion implanted BDD films. SEM images of b) as-grown BDD, c) as-implanted Mn-BDD, d) annealed Mn-BDD thin films (Scale bar ≈500 nm).

Figure 2 represents the optical image of BDD, Mn-BDD, and Mn-BDD$_{AN}$ captured by a confocal laser scanning microscope (CLSM). The topography is displayed together with a 2D and 3D CLSM false-color image maps in which the various colors correlate to the various height profiles of the films. Different height profiling was carried out to calculate the average surface roughness of these films. The average surface roughness (Rq) of the BDD, Mn-BDD, and Mn-BDD$_{AN}$ films wwas calculated as 0.4, 0.281, and 0.103 µm respectively. With ion implantation and subsequent air annealing, the diamond surface gets smoother. On the diamond surface, Ar ion bombardment had a similar effect.[29,30] When the energy of the Mn ions exceeds the atomic displacement in the structure, few ions are very likely penetrated to the interior into the diamond, and the ions energy tends to dissipate into the large volume of the diamond interior. This process results in less surface diffusion of defects and a denser structure with higher compressive stresses and smoother surfaces.[29,30] The same is witnessed in the SEM images as well, the sharp edges of faceted BDD grains were diminished by the implanted Mn ions which results in a much smoother surface. Further annealing process transforms the Mn-BDD grains to irregularly shaped small grains (below 100 nm sizes) and apparently, Mn-BDD$_{AN}$ film shows the lowest surface roughness due to the formation of nano-sized granular grains as evidenced by SEM images as well. The efficacy of the EC reaction is significantly influenced by the formation of nanoclusters in Mn-BDD$_{AN}$ (discussed later).

The growing disorder and the types of defects induced on the BDD surface due to Mn ion incorporation are further analyzed by Raman spectroscopy and X-ray diffraction (XRD) studies. Raman spectrum of BDD thin film (Curve I. in **Figure 3**a) illustrating a sharp and intense first order Raman resonance peak ≈1328.36 cm^{-1} with full width at half maximum ≈15.2 cm^{-1}, demonstrating the sp^3 hybridization of carbon of diamond phase.[31,32] In addition, a broad band centered at 1230 cm^{-1} is attributed to the boron incorporation into the diamond lattice, impurity band formation, and Fano interference.[33,34] However, this broad-band is not associated with the presence of sp^2 carbon.[33] Another broad band centered ≈1550 cm^{-1} is attributed to the G-band of sp^2 hybridization of carbon.[35] The Raman spectroscopy results confirm the presence of non-diamond carbon phases in BDD films at grain boundaries due to high boron doping (B/C ≈10 000 ppm), which leads to secondary nucleation and the formation of a large number of grain boundaries.[25] Amorphization [formation of amorphous carbon (a-C)] of Mn-BDD surface is observed from the Raman spectrum of as-implanted Mn-BDD (Curve II. in Figure 3a), the impact of high dose, high energy, and large mass Mn ions on BDD surface lead to the lethal damage to formation of amorphous carbon.[24] As aforementioned, the implanted Mn ions are distributed up to 90 nm depth and the amorphization is evident in Mn-BDD thin films up to the thickness of 90 nm.

Subsequently, annealing causes the oxidation of Mn clusters on the Mn-BDD surface resulting in the formation of manganese oxide nanoparticles. In addition, the annealing leads to the conversion of a-C to nanographite (Curve III. in Figure 3a) by the catalytic effect of Mn-ions of Mn-BDD thin films.[24,36,37] Annealed Mn-BDD thin film showing a broad Raman resonance peak at 1332.26 cm^{-1} (Curve III. in Figure 3a) is attributed to first order Raman resonance peak, however, the Raman peak is much broader compared to the as-grown BDD (Curve I. in Figure 3a), which indicates the formation of nanocrystalline diamond particles.[38,39] In addition, a shoulder peak to the first-order Raman resonance peak has appeared at 1355 cm^{-1} (Figure 3a), which corresponds to the disordered carbon (D-band).[40] The existence of graphitic (sp^2) carbon phase by the annealing of Mn-BDD was evidenced by the broad Raman resonance peak centered at 1591 cm^{-1} of G-band (Figure 3a), demonstrating a shift from 1550 cm^{-1} (as-grown BDD) to 1591 cm^{-1} (annealed Mn-BDD). The observed blue shift of the G-band in annealed Mn-BDD is owing to the formation of the nanographite phase and stress in the samples.[40]

The X-ray diffraction pattern analysis results of BDD, Mn-BDD, and annealed Mn-BDD samples were shown in Figure 3b. Curve I in Figure 3b depicts the XRD pattern of BDD thin films, which reveals an intense peak centered at 2θ = 44.3° attributed to {111} and a small peak ≈2θ = 75.3° corresponding

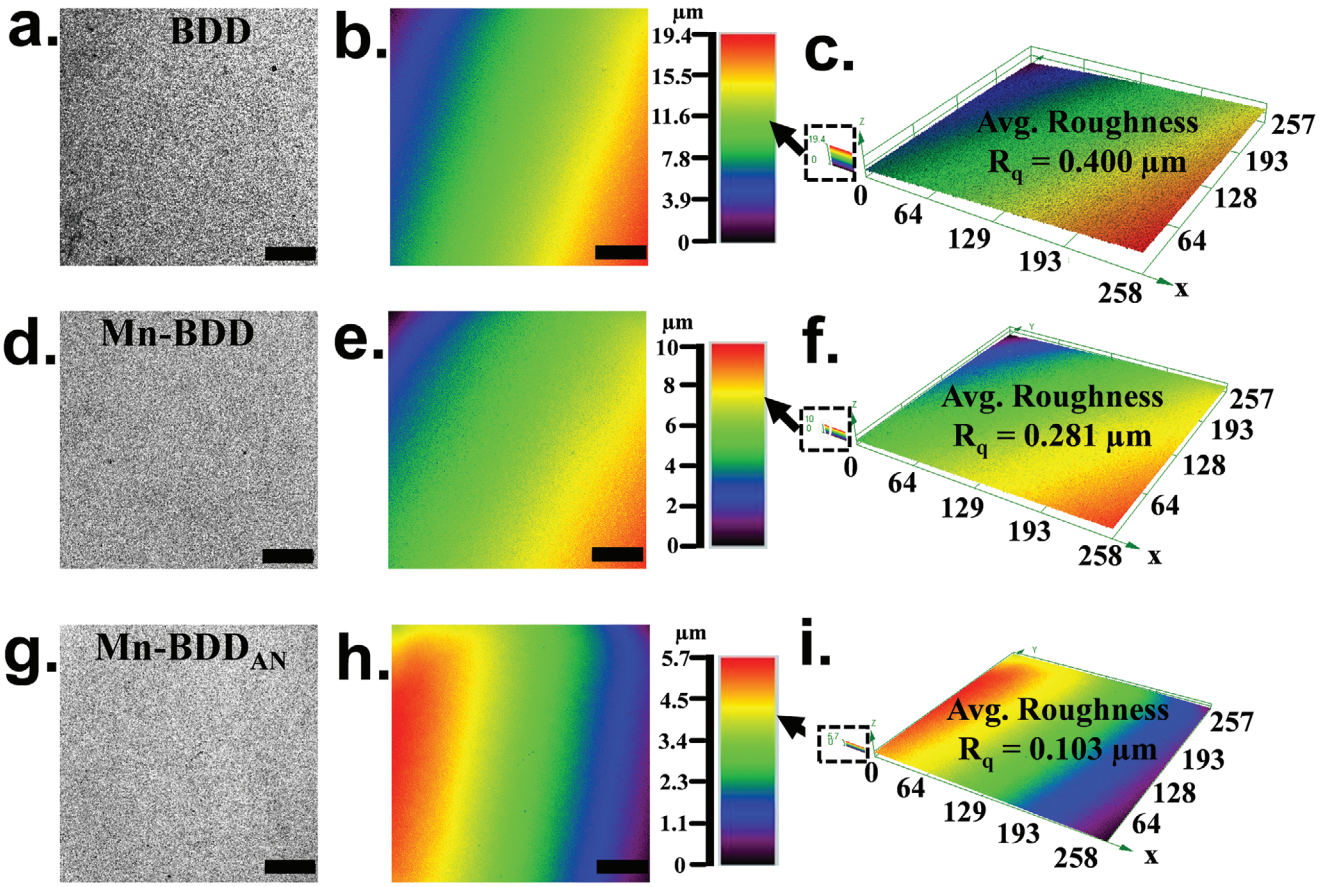

Figure 2. Confocal laser scanning microscope optical image and corresponding false color 2D and 3D image maps of (a,b,c) as-grown BDD, (d,e,f) as-implanted Mn-BDD, and (g,h,i) annealed Mn-BDD thin film. Scale bar ≈50 µm.

to {220} planes of polycrystalline diamond.[14,32] The interplanar spacing of diamond 111 plane (d_{111}) is 0.209 nm, as observed previously.[14] The high intensity of {111} planes is due to an increase in the number of {111} faceted grains by the inclusion of the high boron dopant in diamond growth plasma.[41] The surface morphology and Raman spectroscopy results revealed a significant impact of the implantation and annealing process on Mn-BDD samples. However, the crystallinity of Mn-BDD and annealed Mn-BDD does not alter due to implantation and post-annealing process, which is confirmed by observing the characteristic crystalline planes {111} at $2\theta = 44.3°$ and {220} at $2\theta = 75.3°$ for Mn-BDD (curve II in Figure 3b) and annealed Mn-BDD (curve III in Figure 3b) samples. Crystallite size of BDD, Mn-BDD, and Mn-BDD$_{AN}$ films were also calculated using Scherrer Equation (1).

$$D = \frac{K\lambda}{\beta \mathrm{Cos}\theta} \quad (1)$$

where k is a constant (k = 0.94), λ is the X-rays wavelength (1.54 Å), β is the full width at half maxima, and θ is half of the diffraction angle. The crystallite size was calculated as ≈22 nm, ≈19 nm, and ≈17 nm for BDD, Mn-BDD, and Mn-BDD$_{AN}$ respectively. A systematic reduction of crystallite size is demonstrated here through Mn ion implantation and post-annealing treatment.

Although the regions of MnO_2 clusters are present in the Mn-BDD and Mn-BDD$_{AN}$ films (as evidenced in XPS), they are not detected in XRD measurement. This is likely because MnO_2 particles have amorphous nature and their atomic percentages are too low in comparison to sp^3 carbon.[42]

The carbon-to-oxygen atomic ratio (C/O) was quantitively calculated from the XPS survey scan graph (Figure S2, Supporting Information). The post-annealing treatment on the Mn-BDD film had a considerable impact on its surface oxygen groups as a result the Mn-BDD$_{AN}$ has the lowest C/O ratio of 6.2 when compared to BDD (C/O ≈20) and Mn-BDD (C/O ≈7.3). The results imply that a large number of oxygenated groups were introduced on the Mn-BDD surface during annealing process which led to the higher sheet resistance of Mn-BDD$_{AN}$ surface (discussed in the next section). To clarify it further, the XPS of BDD thin films were collected and deconvoluted high-resolution C 1s, B1s, and O 1s lines are shown in **Figure 4**a–c, respectively.

The deconvoluted C1s core line of BDD thin films consists of four peaks (Figure 4a), which are centered at 285.1 eV from C—C bonding of C-sp^3 carbon (39.5%), 284.8 eV from C≐C bonding of C- sp^2 carbon (53.9%), 286.4 eV from C—O/C—OH (4.6%), and 283.47 eV for B-C sp^3 carbon (1.8%).[43–45] XPS results of C1s are revealing the presence of a high amount of C-sp^2 carbon

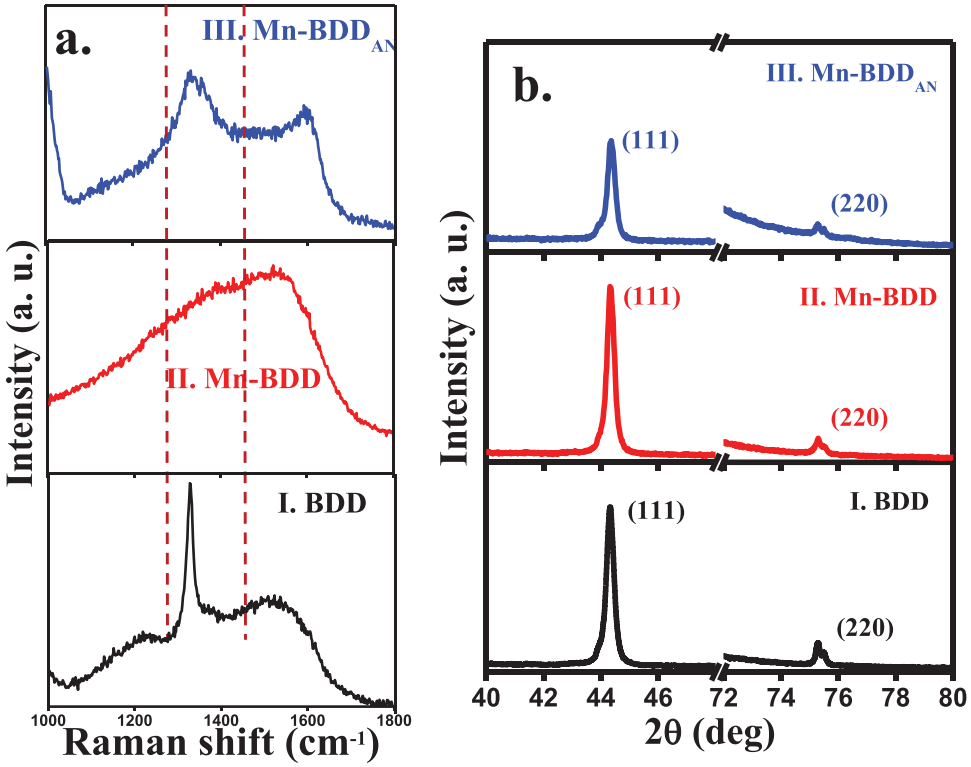

Figure 3. a) Raman spectrum of I. as-grown BDD, II. as-implanted Mn-BDD, III. annealed Mn-BDD thin films, b) XRD pattern of I. as-grown BDD, II. as-implanted Mn-BDD, III. annealed Mn-BDD thin films.

than C-sp^3 carbon, residual C—O/C—OH components and sp^3 carbon of B-C. Figure 4b depicts the deconvoluted B1s peaks at 188.8 eV for B- sp^3 carbon and 186.5 eV for B- sp^3 boron confirming the successful boron doping of BDD thin films.[43] The deconvoluted O1s spectrum of BDD thin films (Figure 4c) indicates two types of oxygenated groups at 532.4 eV and 533 eV for C≐O and C—OH/C—O, respectively.[46–48] High-resolution XPS of the C1s spectrum of Mn-BDD thin films is shown in Figure S3 (Supporting Information). The main constituents of deconvoluted C1s core line of Mn-BDD thin films centered at 285 eV for C—C bonding of C—sp^3 carbon (44.6%), 284.6 eV from C≐C bonding of C- sp^2 carbon (32.9%), 286.8 eV from C—O/C—OH (14.8%) and 288 eV for C≐O (1.8%). The fraction of sp^3 carbon has been increased from 39.5% (BDD) to 44.6% (Mn-BDD) due to the formation of amorphous carbon (mixture of sp^3/sp^2) in the as-implanted Mn-BDD by ion implantation. In addition,

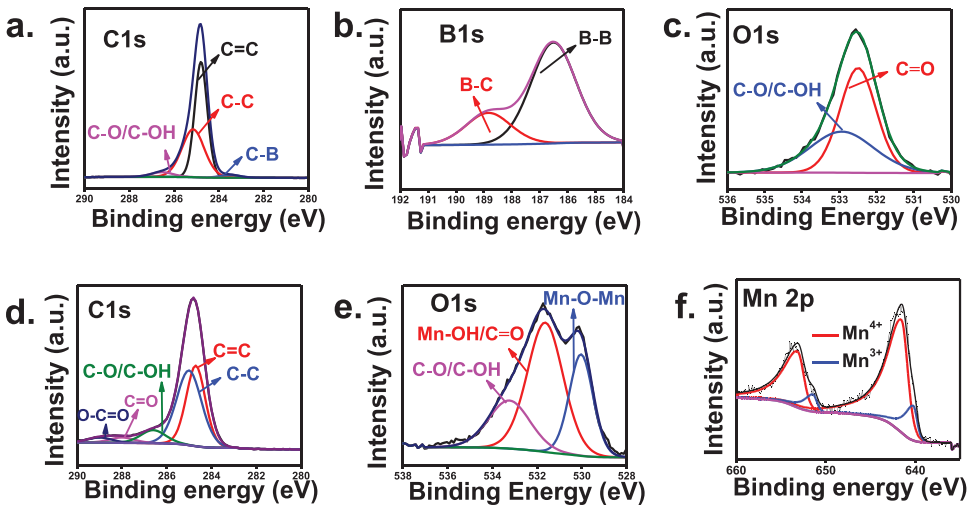

Figure 4. XPS deconvoluted curves of as-grown BDD: a) C1s spectra, b) B1s spectra, c) O1s spectra. XPS deconvoluted curves of annealed Mn-BDD: d) C1s spectra, e) O1s spectra, f) Mn 2p spectra.

carbonyl group C = O centered at 288 eV (7.6%) and enhanced carboxyl group C—O/C—OH (14.8%) was observed for Mn-BDD samples. Figure 4d shows the XPS spectra of the C 1s line of annealed Mn-BDD thin films, which are further deconvoluted into five peaks centered at 285 eV for C—C bonding of C-sp^3 carbon (45%), 284.7 eV for C≐C bonding of C- sp^2 carbon (36.3%), 286.6 eV of C—O/C-OH group (12.5%), 288 eV of C≐O group (3.1%) and 289 eV of O—C≐O (2.9%) group.[43–45] The formation of oxygenated groups like carbonyl/carboxyl groups was enhanced by the annealing process.

Further, the XPS of O1s spectra of annealed Mn-BDD thin films (Figure 4e) were acquired and further deconvoluted into three peaks cantered at 530 eV corresponding to the lattice oxygen (O_{latt}: O_2^{2-}/ Mn—O—Mn); and the other two peaks correspond to the Mn—O—H/C≐O (≈531.7 eV) and C—OH (≈533.3 eV) respectively,[46–48],[49,50] The deconvoluted O1s spectra of Mn-BDD are displayed in Figure S3 (supporting information) where we observed only two oxygen-containing species namely, lattice oxygen (O_{latt}: O_2^{2-}/ Mn—O—Mn) and surface adsorbed oxygen.[49] The relative intensity of O_{latt} in Mn-BDD_{AN} is ≈26%, whereas it is only 6% for the Mn-BDD sample.

The binding energy of XPS Mn 2p core-level spectra is fitted with dominant peak ≈642 eV (Mn $2p_{3/2}$)/≈653 eV (Mn $2p_{1/2}$) and small shoulder peaks ≈641 eV (Mn $2p_{3/2}$)/≈652 eV (Mn $2p_{1/2}$) corresponding to the Mn^{4+} and Mn^{3+} states respectively.[49–51] This indicates the formation of multivalent Mn ions coexisting in the Mn-BDD_{AN} films. Nevertheless, the atomic ratio of Mn^{4+} and Mn^{3+} is ≈85% and ≈15% respectively. The result indicates the MnO_2 phase predominates in the Mn-BDD_{AN} films. Meanwhile compared to MnO_2 phase-dominated Mn-BDD_{AN} films the positive shifts of Mn 2p peaks are observed for Mn-BDD films (Figure S3, Supporting Information) and the atomic ratio of Mn^{4+} and Mn^{3+} is ≈20% and ≈80% respectively. These results provide evidence of phase change from Mn^{3+} dominated Mn-BDD to Mn^{4+} dominated Mn-BDD_{AN} films just by annealing process.

The microstructural analysis using high-resolution transmission electron microscopy (HRTEM) further validates the existence of a diamond lattice within Mn-BDD and Mn-BDD_{AN} films. The detailed microstructures of regions 1 and 2 in **Figure 5**a,d are clarified by the HRTEM micrograph in Figure 5b,c,d,f respectively. In typical HRTEM images (Figure 5b,e) of the Mn-BDD and Mn-$BDD_{AN,}$ identifiable diamond lattice planes {111} are observed. The gap between two successive fringes measures approximately 0.21 nm, aligning closely with the dimensions of diamond {111} planes found in nanodiamond crystals.[14,32] Additionally, there is an evidence of amorphous carbon (Figure 5c) and graphitized layers (Figure 5f, interlayer spacing is ≈0.37 nm) forming along the grain boundaries of the diamond crystallites of Mn-BDD and Mn-BDD_{AN} respectively.

The cross-sectional microstructures of the Mn-BDD and Mn-BDD_{AN} films were further illustrated by the composed bright field TEM images (Figure 5 g,m) while the corresponding high-angle annular dark-field (HAADF) images were displayed in Figure 5h,n respectively. The approximate film thickness of the Mn-BDD and Mn-BDD_{AN} films was determined to be ≈1.33 µm and 1.25 µm respectively. Elemental mapping of C—K, O—K, and Mn—K, acquired from the marked squares in Figure 5h,n respectively, reveals the evident C, O, and Mn in both Mn-BDD and Mn-BDD_{AN} films, where Mn-K elements were found at an approximate depth of >100 nm. These observations correspond well with the anticipated penetration depth (d_p) of Mn ions, as calculated through simulations utilizing the Stopping and Range of Ions in Matter approach.

The surface porosity, chemical functionality, and microstructure play a crucial role in controlling film resistance. BDD (57.42 Ω square^{-1}) and Mn-BDD (53.95 Ω square^{-1}) samples have similar sheet resistance (Figure S5, Supporting Information) but interestingly a significant increase in the sheet resistance was observed for Mn-BDD_{AN} sample (193.92 Ω square^{-1}). The lowest sp^2/sp^3 carbon ratio, increased proportion of oxygen functional groups, formation of MnO_2 phase and more porous granular structure make the Mn-BDD_{AN} sheet resistance high. The defect induced Mn-BDD_{AN} surface with a larger degree of oxygen functional group, which promotes the electrolyte to sink into the porous structure plays an important role in EC SC performance which is discussed next.

Figure S6 (Supporting Information) shows the water contact angle values of the BDD, Mn-BDD, and Mn-BDD_{AN} samples. The WCA values are observed as BDD_{WCA} (≈120°) > Mn-BDD_{WCA}(≈85°) > Mn-BDD_{AN} (≈61°). The reduction in contact angle for the Mn-BDD_{AN} is explained based on the surface chemical state. The association between WCA and oxygen content can be explained by the well-known fact that C—O/C—OH and C≐O bonds are more polar than C—C and C—H bonds.[52,53] The increased proportion of hydroxyl group and lattice oxygen on the Mn-BDD_{AN} surface (as evidenced by the XPS observations) improve its hydrophilicity and facilitate better contact with the electrolyte, which is one of the reasons for better SC performance as compared to other films.

To understand the effect of Mn ion implantation on the electronic structure of BDD, we ran a series of theoretical simulation which is presented below.

2.2. Theoretical Simulations

Molecular structures of diamond, BDD, Mn-diamond and Mn-BDD models were designed using a builder tool provided by Atomistic ToolKit Quantumwise (ATK, Synopsys, USA) package as reported in [Atomistix Toolkit Version 2019.03, Synopsys QuantumWise A/S (Www.Quantumwise.Com]. Density functional theory (DFT) on the generalized gradient approximation (GGA) level of theory with the Perdew–Burke–Ernzerhof (PBE) functional was applied as implemented in the package. The Linear Combination of Atomic Orbitals (LCAO) method with the[54] Pseudo Dojo scalar relativistic pseudopotentials were applied.[55] The Fermi-Dirac occupation scheme is used throughout the work. The details can be found in the supporting information file.

2.3. DFT-Based Band Structure Analysis

In order to investigate the influence of the Mn implantation on the electronic structure inside the bulk of the supercapacitive material, a series of band structure calculations have been performed using DFT (**Figure 6**). In general, pristine diamond

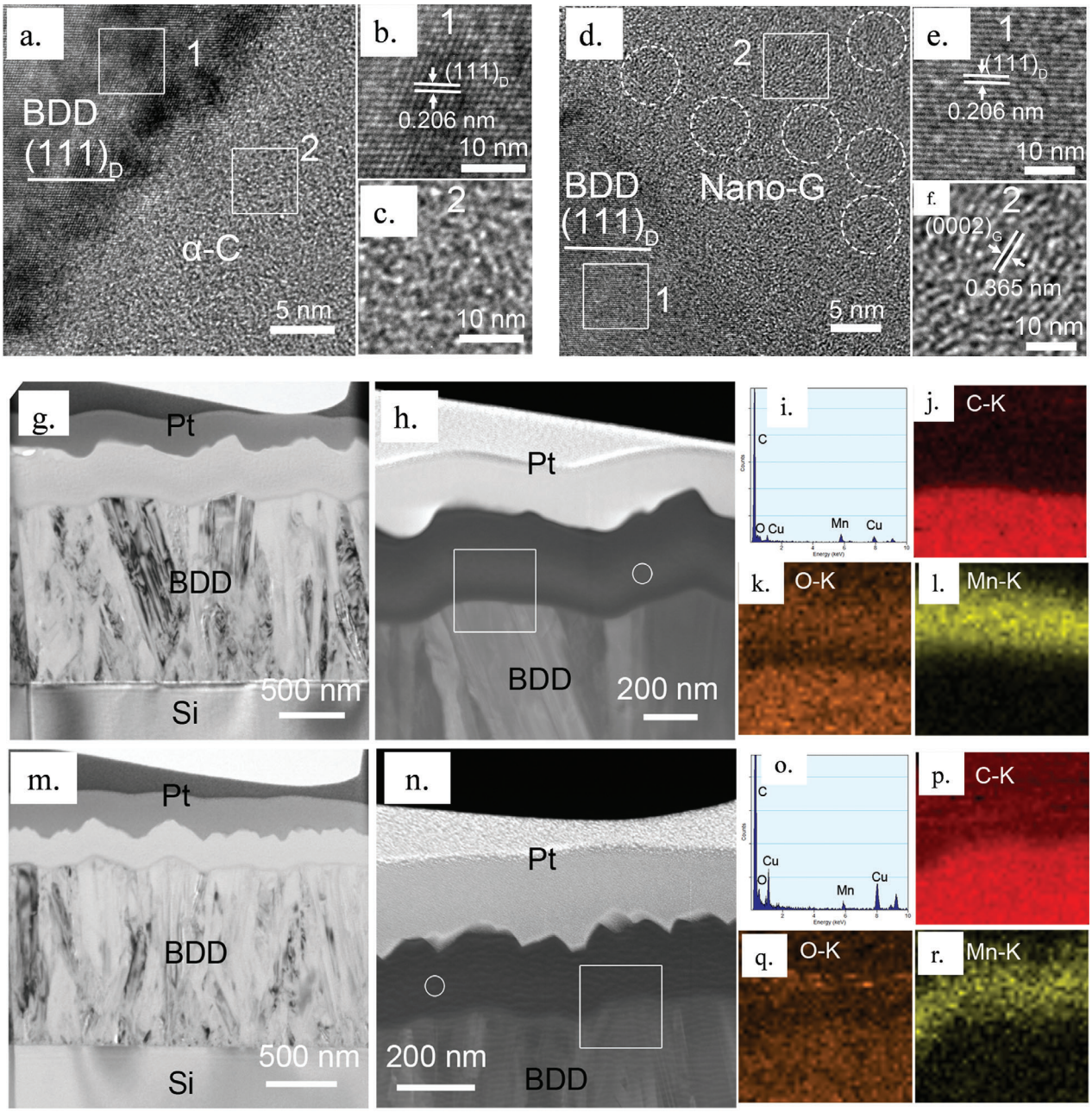

Figure 5. a) Cross-sectional HRTEM image of the surface layer in as-implanted Mn-BDD sample taken along the [110] zone axis of diamond; b) Magnified HRTEM image of the region 1 in a), indicating the presence of diamond; c) Magnified HRTEM image of the region 2 in a), indicating the presence of amorphous carbon above the diamond layer. d) Cross-sectional HRTEM image of the surface layer in Mn-BDD_{AN} sample taken along the [110] zone axis of diamond; e) Magnified HRTEM image of the region 1 in d), indicating the presence of diamond; f) Magnified HRTEM image of the region 2 in d), indicating the presence of nanographite above the diamond layer. Cross-sectional microstructures of the surface layer in the as-implanted Mn-BDD sample (g-l) and the Mn-BDD_{AN} sample (m-r): (g, m) TEM bright-field images; (h, n) corresponding HAADF images; (i,o) EDS spectra taken from the marked circles in (h) and (n),respectively; element mapping of C-K (j,p), O-K (k,q) and Mn-K (l,r) taken from the marked squares in (h) and (n) respectively.

exhibits typical direct bandgap equal to 5.85 eV at the gamma point with the Fermi level located inside the gap (subfigure a). In the case of BDD, there is a set of additional electronic levels originating mainly from electron density of boron dopants located close to the valence band edge (subfigure c). Considering the Fermi level crosses one of those bands, and its E-k dispersion is relatively high, BDD is conductive. However, when an Mn atom is introduced instead of the BDD a whole set of new energy levels are introduced inside the gap and the Fermi level crosses one of them (subfigure b). Therefore, Mn can be classified as an n-type dopant for diamond. These are exactly five bands originating from five d-type orbitals of the Mn valence shell exhibiting

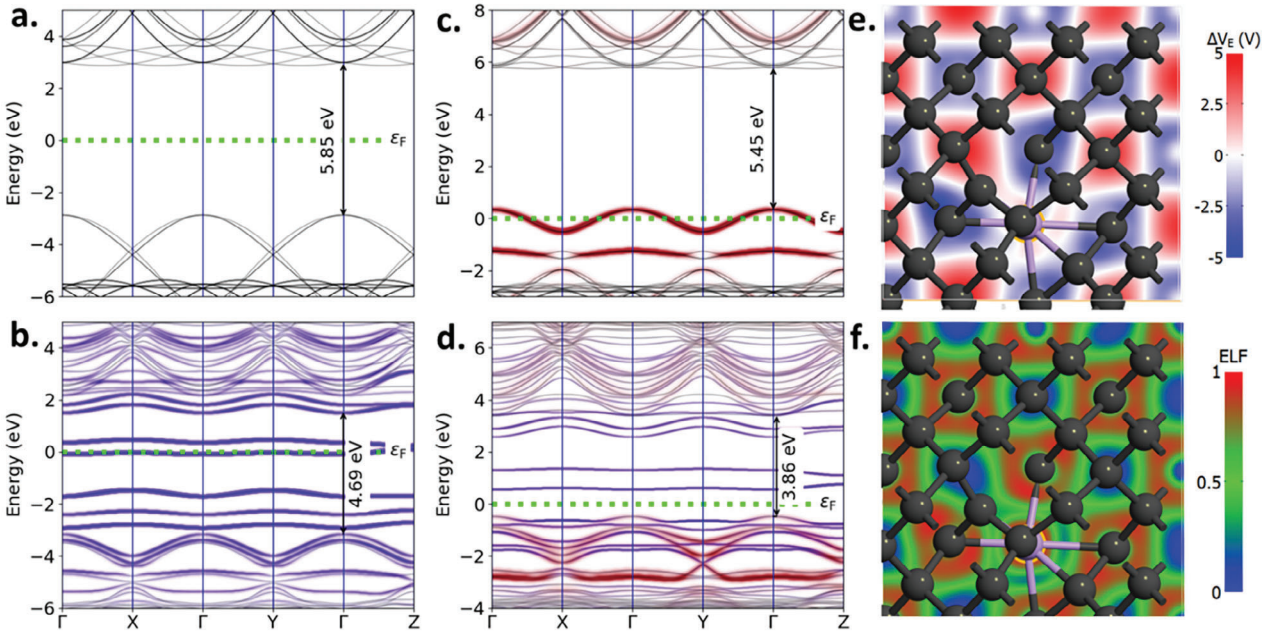

Figure 6. DFT-based band structure calculations of the a) pristine diamond, b) Mn-doped diamond, c) BDD and d) Mn-doped BDD; e) electrostatic difference potential map and d) electron localization function map in the vicinity of the Mn dopant in the diamond unit cell. Black lines correspond to projections form carbon molecular orbitals, red from boron and blue from Mn.

small E-k dispersion and therefore are expected to be poorly conducting compared to the boron dopants. Interestingly, after incorporation of the Mn into the lattice, its levels strongly overlap with orbital energies belonging to the carbon atoms initially (visually, there is a mixing of the blue and black colors of the bands constituting the VB and CB). In other words, Mn orbitals are delocalized in the momentum space, while boron levels are localized. This would indicate that in the real space electronic states of Mn are localized and states of boron are highly conductive. Finally, when both dopants are introduced to the unit cell together (with 1:1 ratio) both Mn and boron energy levels appear on the band structure diagram (subfigure d). The Fermi level is shifted to the valence band edge with respect to the pristine diamond, but is markedly elevated compared to the BDD. Despite in case of single dopants (both Mn and B) the Fermi level crosses occupied bands, when both dopants are present it crosses the gap again. Briefly, Mn doping counteracts B doping.

The discussed band structures are obtained after the unit cell is geometry optimized with relaxed cell parameters and symmetry constraints. After optimization, the Mn atom resides in an interstitial position and has coordination number equal to 8. The lattice parameters are slightly changed from 7.134 × 7.134 × 7.134 Ang^3 (all right angles and cubic diamond symmetry) to 7.268 × 7.269 × 7.233 Ang^3 (90.3 deg x 89.7 deg x 91.5 deg). As a result, the local environment of the Mn site is strongly distorted and diamond symmetry is lost – the cell is triclinic. Movie S1 shows animated frames from the unit cell optimization trajectory.

To further explore the properties of the Mn dopant, electrostatic difference potential (EDP) and electron localization function (ELF) maps have been calculated and plotted in the plane containing Mn dopant (subfigures e and f respectively). In this plane, all carbon atoms exhibit negative charges and positive charges correspond to the voids between atoms. However, the Mn site exhibits positive electrostatic potential compared to its carbon neighbors suggesting that it acts as an electron donor to the lattice (n dopant). It is also confirmed by the Mulliken analysis, which yielded 6 valence electrons (Mn^{+}) before and 5.196 valence electrons (Mn^{2+}) after incorporation into the lattice. On the other hand, the ELF map shows localization of the charge onto the Mn atom (red circle) with a cloud of slightly delocalized charge in its vicinity (greenish circles). Although Mn electronic states have a finite conductivity, this partial localization suggests that the boost is smaller compared to the boron doping, which is in line with the inferences from the band structure (i.e., smaller E-k dispersion).

2.4. Non-Eqiullibrium Green's Function (NEGF) Calculations of the Electronic Transmission

Furthermore, fully periodic Mn-BDD cells have been used to build device configurations with Dirichlet boundary conditions in the Z-direction allowing NEGF formalism to be applied. Projected local density of states (PLDOS) and electronic transmission spectra have been computed for the pristine BDD cell or Mn-doped BDD cell sandwiched between two other BDD cells as depicted in **Figure 7**a. In the former case, these are 3 boron dopant atoms, in the latter, 2 boron and 1 Mn dopants are present. The distance on the x axes of the PLDOS plot corresponds to the length of the scattering region, i.e., BDD or Mn-BDD cell.

PLDOS map of the pristine BDD clearly shows that the Fermi level is shifted to the valence band edge and the 5 eV bandgap is preserved in the device configuration (subfigure b). High

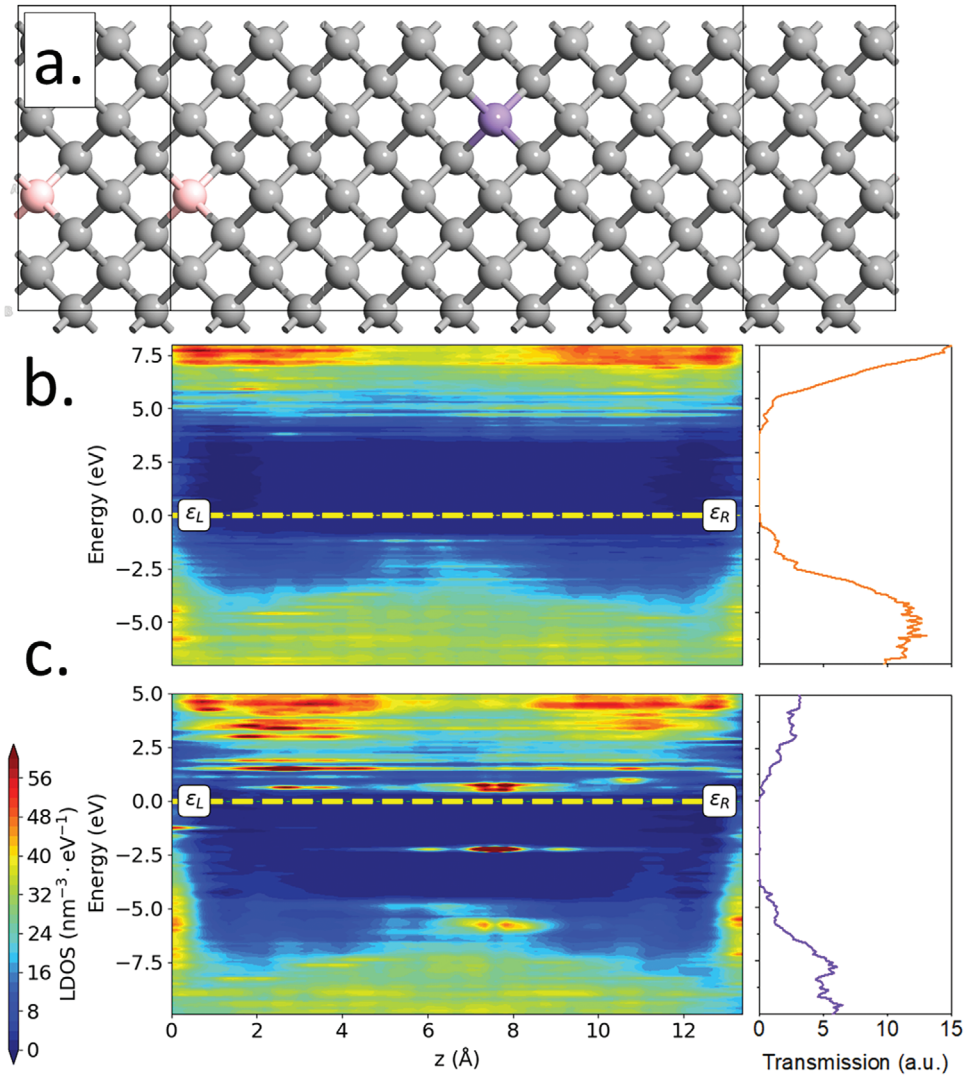

Figure 7. NEGF electronic structure calculation of the Mn-doped BDD; a) geometry of the junction, b,c) PLDOS and the corresponding transmission spectrum of the BDD and Mn-doped BDD respectively.

values of the transmission in the vicinity of the Fermi level confirms high conductance. On the other hand, the Fermi level is significantly elevated towards the CB edge, when the Mn-BDD cell is in the scattering region. Surprisingly, a single Mn dopant is capable of counteracting two boron dopants and switching the junction character form the p-type to n-type in the presented simulation. Additional Mn d-orbital energy levels in the middle of the gap are preserved, though.

Summarizing the DFT contents and considering the lack of literature on Mn doped diamond it is possible to speculate that two factors, i.e., low E-k dispersion and charge localization contribute to the lower sheet resistance of the Mn-doped BDD samples.

2.5. DFT Calculations of Raman Spectra

Additional DFT simulations of Raman spectra for the pristine diamond, BDD, Mn-doped diamond and Mn-doped BDD have been included in the Supporting Information file (Figure S4, Supporting Information). The pristine diamond exhibits several well-defined bands constituting the experimentally observed D band. Introduction of the boron leads to the manifestation of several normal modes involved in the C-B bonds effectively broadening the band below 1200 cm^{-1}. This behavior is consistent with the literature.[56,57]

However, incorporation of the Mn into the lattice leads to profound alteration of the Raman spectrum, as many bands emerge in the region between 1000 and 1300 cm^{-1}. Considering that in the vicinity of an Mn atom the coordination sphere is strongly distorted, the symmetry is broken and initially Raman inactive modes become active due to the symmetry breaking.[40] Similar behavior is observed when both dopants are present in the lattice. Although graphitization can happen and lead to shifts of the G band, the experimental changes of the D band shape might be caused by this symmetry breaking as a result of a mere act of Mn insertion in the implantation process.

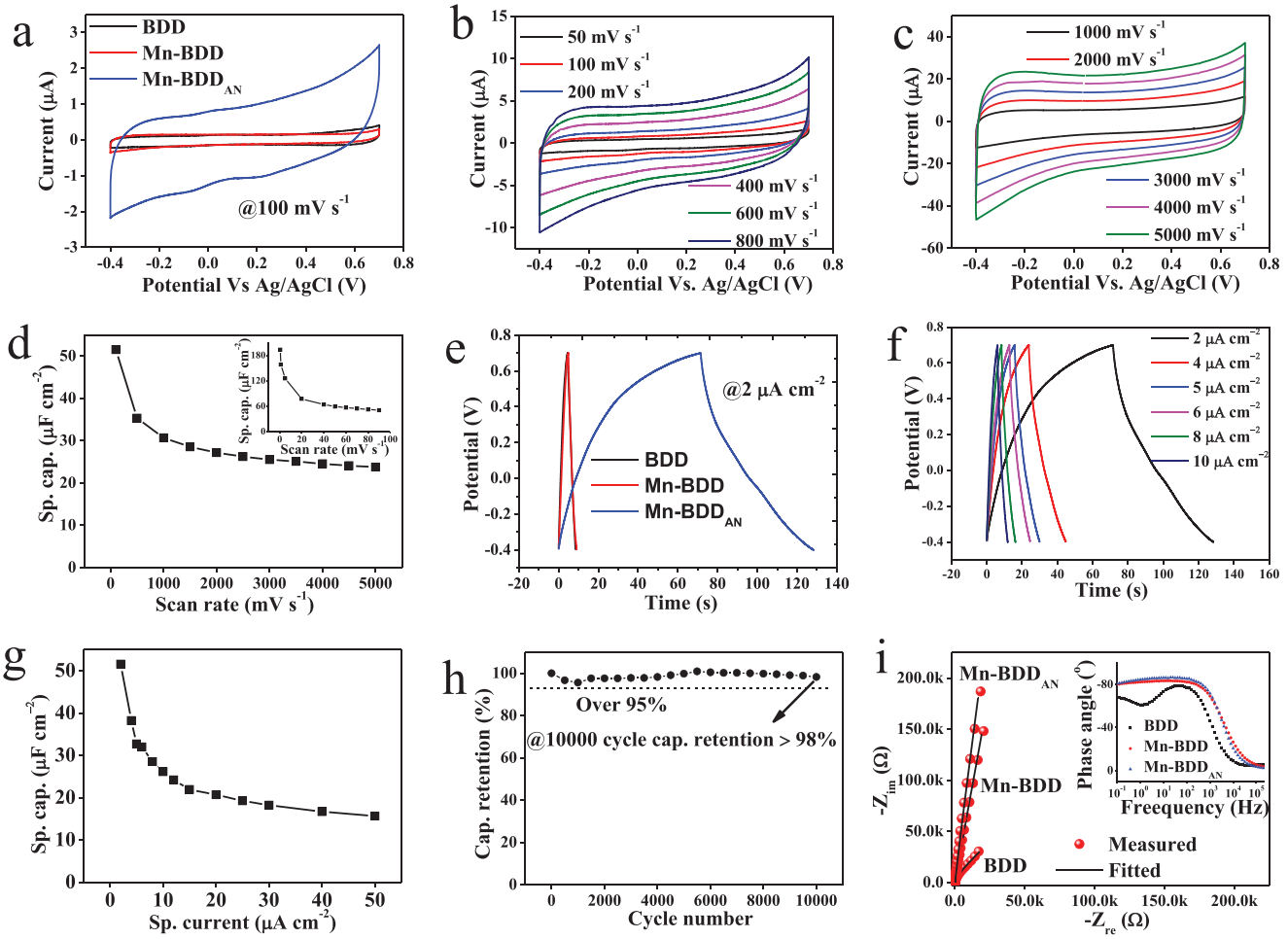

Figure 8. Electrochemical performance in 1 M Na_2SO_4 aqueous solution. a) Comparative cyclic voltammograms of BDD, Mn-BDD, and Mn-BDD_{AN} at a scan rate of 100 Mv s^{-1}. b) and c) Rectangular cyclic voltammograms (EDLC) of Mn-BDD_{AN} at varying scan rates ranging from 50 to 5000 mV s^{-1}. d) Areal-specific capacitance of Mn-BDD_{AN} as a function of scan rates. e) Comparative galvanostatic charge-discharge curves of BDD, Mn-BDD, and Mn-BDD_{AN} at a current density of 2 μA cm^{-2}. f) Triangular galvanostatic charge-discharge curves (EDLC) of Mn-BDD_{AN} with varying current density. g) Areal-specific capacitance of Mn-BDD_{AN} as a function of current density. h) Cyclic stability of Mn-BDD_{AN}. Capacitance retention ≈98% after 10000 charge-discharge cycles. i) Experimental and fitted electrochemical impedance spectra of BDD, Mn-BDD, and Mn-BDD_{AN} within the frequency range of 0.1 Hz to 1 MHz with inset showing corresponding Bode plot.

2.6. Electrochemical Supercapacitor Performance

To illustrate its potential applicability of annealed Mn implanted BDD for the fabrication of SC, its capacitive behavior was tested using three-electrode system using both aqueous (1 M Na_2SO_4) and redox species containing aqueous (0.05 M $Fe(CN)_6^{3-/4-}$ + 1 M Na_2SO_4) electrolyte. The EC performance was assessed utilizing cyclic voltammetry (CV) as well as galvanostatic charge-discharge (GCD) tests. Compared with BDD and Mn-BDD, the annealed Mn-BDD (Mn-BDD_{AN}), exhibits improved EC performance with a quasi-rectangular CV shape (**Figure 8**a), indicating the characteristics of electrical double-layer (EDL) capacitor. Interesting to note that, the Mn-BDD_{AN} is robust enough to maintain the ideal rectangular CV curve over a wide range of scan rates (100–5000 mV s^{-1}, Figure 8b,c). However, at the low scan rates (< 50 mV s^{-1}), there were weak redox peaks corresponding to the Faradaic current associated with the redox reaction of $Mn^{3+/4+}$ canters (Figure S7, Supporting Information). The estimated capacitances are ≈ 159, ≈ 77, and ≈ 51 μF cm^{-2} at a scan rate of 1, 20, and 100 mV s^{-1} respectively (Figure 8d).

Figure 8e shows the comparative GCD curves of BDD, Mn-BDD, and Mn-BDD_{AN} at a current density of 2 μA cm^{-2}. The longest discharge period again demonstrates the superiority of Mn-BDD_{AN} over BDD, and Mn-BDD films. The GCD curves Mn-BDD_{AN} with varying current density show a fair triangular shape (Figure 8f), indicative of the formation of efficient EDL with excellent reversibility. The voltage loss (IR drop) is barely perceptible at all of these applied current densities due to the good conductivity of the Mn-BDD_{AN} films and improved electrolyte contact at the electrode-electrolyte interface. The specific capacitance was calculated using the GCD curves across a wide range of applied current densities (Figure 8g; Figure S8, Supporting Information). At current densities of 5, 20, and 100 μA cm^{-2}, the calculated capacitances are ≈ 33, ≈ 25, and ≈ 16 μF cm^{-2}, respectively. The cyclic stability of the Mn-BDD_{AN} films was next investigated as an important characteristic for real-life SC applications, and the results

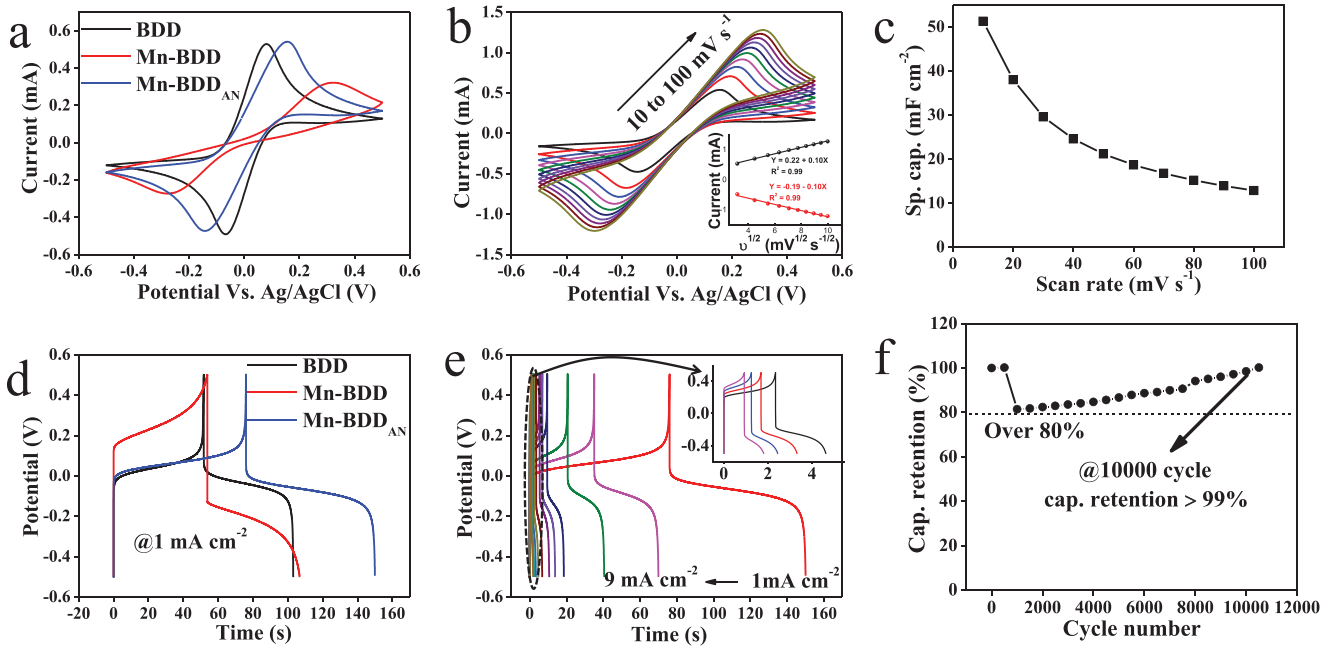

Figure 9. Electrochemical performance in redox active electrolyte of 0.05 M $Fe(CN)_6^{3-/4-}$ contained 1 M Na_2SO_4 aqueous solution. a) Comparative cyclic voltammograms of BDD, Mn-BDD, and Mn-BDD_{AN} at a scan rate of 10 mV s^{-1}. b) Cyclic voltammograms of Mn-BDD_{AN} at varying scan rates ranging from 10 to 100 mV s^{-1} with inset showing the variation of the anodic and cathodic peak currents as a function of the scan rate. Pseudocapacitive redox peaks are visible. c) Areal-specific capacitance of Mn-BDD_{AN} as a function of scan rates. d) Comparative galvanostatic charge-discharge curves of BDD, Mn-BDD, and Mn-BDD_{AN} at a current density of 1 mA cm^{-2}. e) Galvanostatic charge-discharge curves of Mn-BDD_{AN} with varying current density. Inset showing the magnified GCD curves at high current density. f) Cyclic stability of Mn-BDD_{AN}. Capacitance retention ≈100% after a 10000 charge-discharge cycle.

are shown in Figure 8h. Outstanding cyclic stability (>98%) was maintained even after the 10 000 charge/discharge cycle.

The EC impedance spectra (EIS) again reveal the superior capacitive behavior of Mn-BDD_{AN} over BDD, and Mn-BDD electrode (Figure 8i). Note that, the Mn-BDD_{AN} displayed larger slope in the low-frequency region as compared to BDD, and Mn-BDD electrodes. The Nyquist plot for Mn-BDD_{AN} is closest to and nearly parallel to the Y axis in the low-frequency zone, showing the best capacitive properties.[14,58,59] Furthermore, the Bode plot shows that Mn-BDD_{AN} has the highest phase angle (≈−80°) at low frequencies (0.1 Hz to 100 Hz) than Mn-BDD and BDD, confirming that Mn-BDD_{AN} characteristics are closer to the ideal capacitor.[59,60]

To improve the capacitive performance of diamond-based thin films even further, we created pseudocapacitances (PCs) by dissolving 0.05 M $Fe(CN)_6^{3-/4-}$ in 1 M Na_2SO_4 aqueous solution. **Figure 9**a shows the anodic and cathodic peak potential separation (ΔE_P) is highest for Mn-BDD (ΔE_P = 0.58 V) and it is lowest for BDD (0.15 V). Interesting to note that ΔE_P value of Mn-BDD_{AN} is ≈0.28 V which is closer to the pure BDD sample. This result indicates the electron transfer of $[Fe(CN)6]^{3-/4-}$ at Mn-BDD_{AN} surface required a larger driving force compared to BDD. This decrease in electron transfer kinetics can be explained based on attached surface oxygen functionalities on the Mn-BDD_{AN} surface which exhibit a thicker depletion layer compared to pure BDD.[61] It is also known that the oxygen sites showed repulsion to the $[Fe(CN)6]^{3-/4-}$, preventing it to adsorb on the electrode surface and thus inhibiting the electron transfer between the redox couple and diamond surface.[62] Interesting to note that in contrast to BDD and Mn-BDD, Mn-BDD_{AN} has the largest oxidation peak intensity of 0.54 mA demonstrating its superiority in capacitive performance. Meanwhile, the peak currents (oxidation and reduction) for Mn-BDD_{AN} are linearly proportional to the square root of the scan rate (inset of Figure 9b) indicating the diffusion-controlled electron transfer kinetics. However, the separation between two redox peak potentials increases further as scan rates increase indicating a quasi-reversible electron transfer mechanism of $Fe(CN)_6^{3-/4-}$ on the electrode surface. The evaluated areal capacitances are ≈13, ≈22, and ≈52 mF cm^{-2} at a scan rate of 100, 50, and 10 mV s^{-1} respectively (Figure 9c).

The related GCD graphs of BDD, Mn-BDD, and Mn-BDD_{AN} displayed nonlinear shapes with a plateau region (Figure 9d) confirming the characteristics of pseudocapacitive charge storage mechanism due to the redox reaction of $Fe(CN)_6^{3-/4-}$. The specific capacitances of Mn-BDD_{AN} estimated by integrating the GCD curves are 37, 14, and 4 mF cm^{-2} at the current density of 1, 3, and 9 mA cm^{-2} respectively (Figure S9, Supporting Information file). Note that, the capacitance values obtained from CV and GCD tests with redox active electrolyte are approximately three orders of magnitude higher than those obtained without redox active electrolyte. The areal-specific capacitance values of Mn-BDD_{AN} electrodes are comparable to or even higher than previously developed diamond-based supercapacitors (Table S1, Supporting Information).

Finally, as a case study, the cyclic stability of Mn-BDD_{AN} was tested using a cycle number of 10000 and a current density of 2 mA cm^2. Notably, after a steep drop after 1000 GCD cycles,

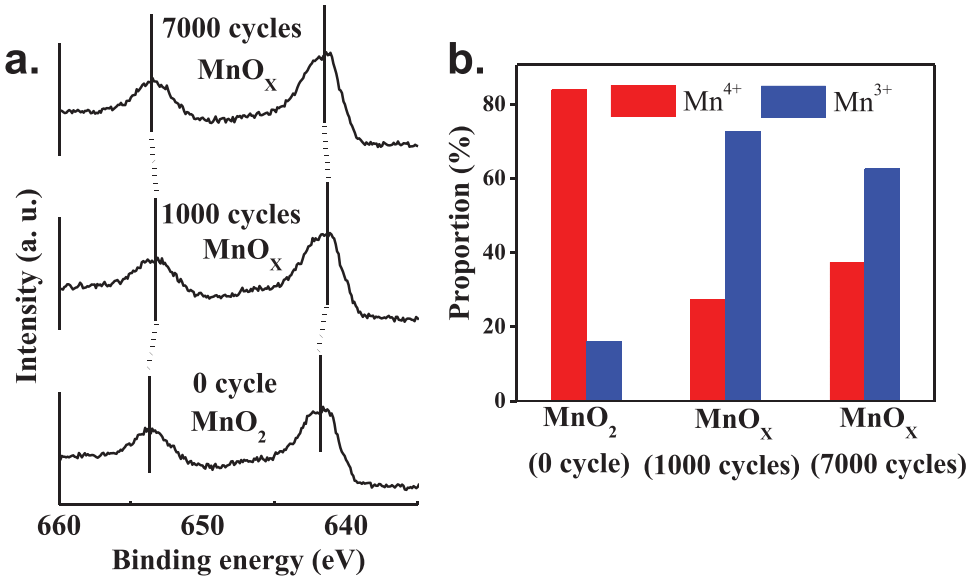

Figure 10. a) Core level XPS Mn 2p spectra for the sample MnO_2 (Mn-BDD_{AN}), MnO_x electrode after 1000 and 7000 cycles. b) The proportion distribution of Mn^{3+} and Mn^{4+} on the surface of MnO_2 (Mn-BDD_{AN}) and MnO_x electrodes after 1000 and 7000 cycles.

the capacitance gradually increases up to 10 000 cycles but does not stop (Figure 9f). The capacitance decrease in the initial cycles could be attributed to structural degradation caused by repeated intercalation/deintercalation of electrolyte ions. After a given cyclic period (1000 cycles), the redox electrolyte soaked into the electrode surface promotes ion intercalation/deintercalation, resulting in an easier redox reaction on the electrode surface. To better understand the above-mentioned explanation, additional ex-situ XPS measurements were carried out of Mn-BDD_{AN} after 1000 and 7000 cycles. **Figure 10**a illustrates the distribution of Mn ions valence states in three different cyclic periods and the relative proportion of Mn^{4+} and Mn^{3+} ions are displayed in Figure 10b. The Mn-BDD_{AN} sample (denoted as MnO_2) is mostly dominated by Mn^{4+} ions (82%) as discussed previously as well. After 1000 cycles, the relative proportion of Mn^{4+} decreased to ≈28% and while the relative proportion of Mn^{3+} increased to ≈72%. Meanwhile compared to MnO_2 the positive shifts of Mn 2p peaks are observed after 1000 cycles. It's worth noting that after 7000 cycles, the Mn 2p peaks have shifted slightly to the left, indicating that the Mn peaks are approaching the initial MnO_2 positions, which is further confirmed by the increased proportion of Mn^{4+} ions (≈38%). Wang et al. also explained a similar kind of GCD behaviour with valence state adjustment of vanadium oxide (VO_x).[59] Therefore, a slight adjustment of Mn valence state is very likely the reason for the exciting phenomenon that capacitance rises gradually with cyclic processes.

The mechanism of the over-time capacitance increase can be explained based on the band-structure perspective as well. In general, XPS results (Figure 4f) and CV curves in the absence of redox mediators (Figure S7) evidence that the initial, as-prepared sample contains some amount of Mn^{3+} besides Mn^{4+}. Moreover, there is no full reversibility and symmetry of the Mn^{3+} / Mn^{4+} redox process (Figure 8a – oxidation currents are slightly higher ≈20 μA cm^{-2}). Due to the lack of symmetry, there is presumably a non-zero amount of Mn^{4+} states on the surface that is formed during each anodic polarization from the initial Mn^{3+} (besides the main oxidation of the redox marker).

An increase in pseudo-capacitance can also occur as a result of Mn^{4+} states accumulation. As mentioned in the DFT part (Figure 6 and 7), the Mn dopant itself seems to counter the effect of boron doping by moving the Fermi level up. However, oxidation of Mn^{3+} to Mn^{4+} is equivalent to shifting the Fermi level back down (electron withdrawal)–as a result, this initial counteraction is minimized. If that is true, there is a slight increase in the charge transfer rate each cycle, as the electron tunnelling probability increases due to boron doping being less hindered. Since the increase in pseudo-capacitance and retention over time.

A ragone plot for energy density and power density of the Mn-BDD_{AN} electrodes with two different aqueous electrolytes (1 M Na_2SO_4 and 0.05 M $Fe(CN)_6^{3-/4-}$ + 1 M Na_2SO_4) is shown in Figure S10 (Supporting Information file). Compared to 1 M Na_2SO_4, the SC performance of the Mn-BDD_{AN} considerably increased when the electrolyte contained a redox pair. The fabricated SC with and without redox couple delivered a maximum energy density of 6.25 and 0.008 μWh cm^{-2} and a maximum power density of 2.29 and 0.07 mW cm^{-2}, respectively.

To demonstrate the potential use of the Mn-BDD_{AN} in producing a miniature energy storage device, we further assembled the Mn-BDD_{AN} into a solid-state supercapacitor configuration using a gel electrolyte (mixture of poly(vinyl alcohol) (PVA) and sulfuric acid). To prepare the solid-state SC device, polymer gelled electrolyte was drop cast on the Mn-BDD_{AN} surface without any binder, separator, or any packaging material (**Figure 11**a). The CV curves of the SC device at varying scan rates (1 to 1000 mV s^{-1}) have an almost rectangular shape within 0 to 1 V (Figure 11b,c) revealing the electrode's pure EDLC behavior. The specific capacitance with varying scan rates is displayed in Figure S11 (Supporting Information). The triangular GCD curves (Figure 11d) further confirm the typical EDLC characteristics and effective charge storage capacity. Figure 11e illustrates that the specific

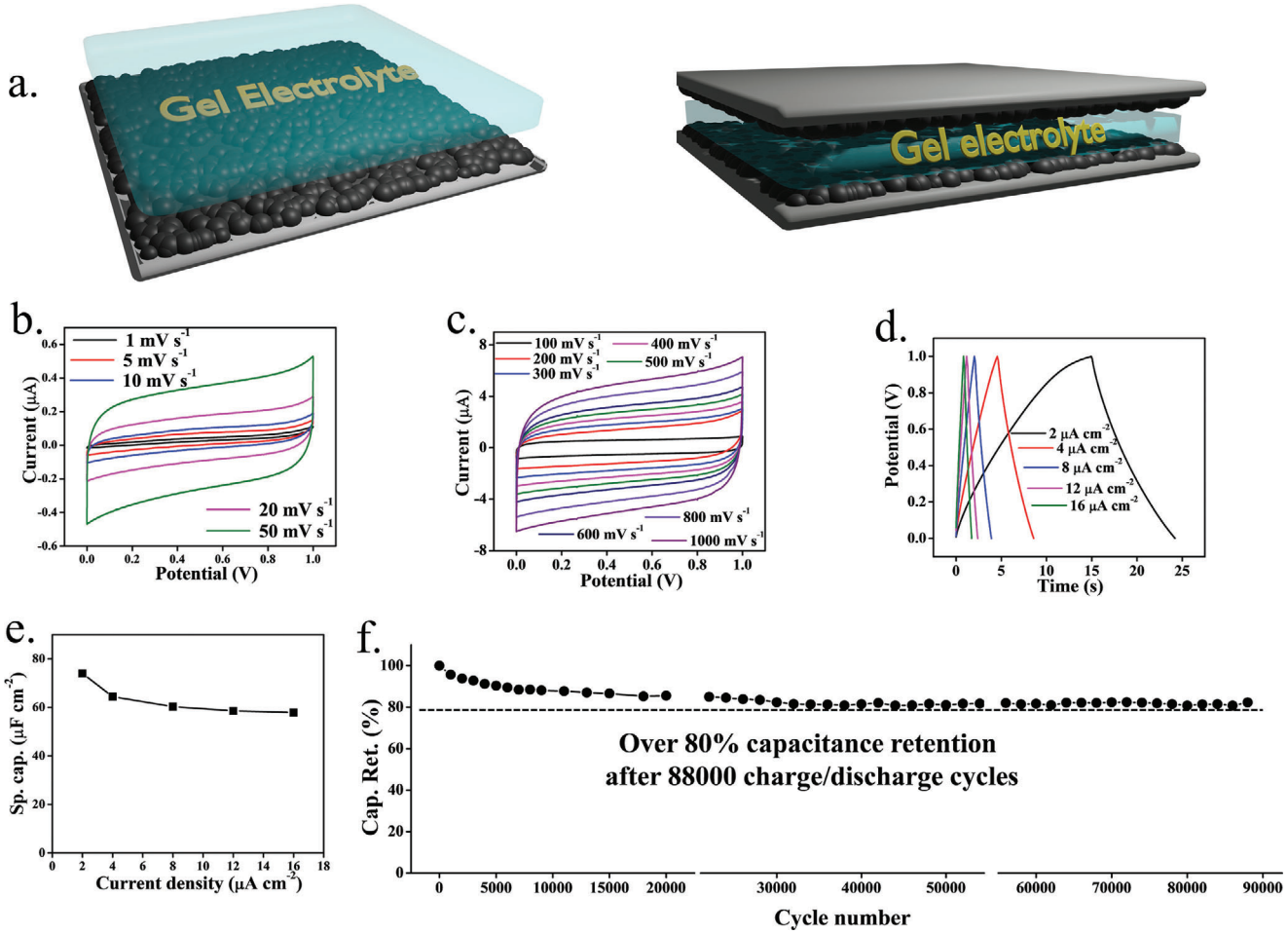

Figure 11. Electrochemical performance of a SC device in PVA-H_2SO_4 gelled electrolyte. a) Schematic fabrication process of the sandwich-SC device. b,c) Cyclic voltammograms of Mn-BDD_{AN} at varying scan rates ranging from 10 to 1000 mV s^{-1}. d) Galvanostatic charge-discharge curves of Mn-BDD_{AN} with varying current density. e) Areal-specific capacitance of Mn-BDD_{AN} as a function of current density. f) Cyclic stability of Mn-BDD_{AN}. Capacitance retention ≈82% after 88000 charge-discharge cycles.

areal capacitance of the SC device is ≈74 μF cm^{-2} at 2 μA cm^{-2} and it retains 80% of its initial capacitance despite an increase in current density of 8 times, indicative of excellent rate response. Figure 11f. reveals that the SC sustained ≈82% of its initial capacitance after 88000 GCD cycles, exhibiting its remarkable performance stability over a long cycle life. To our knowledge, this is the best cyclic stability reported till date for any diamond-based SC devices (Table S2, Supporting Information file).

Figure S12 (Suppoting Information) in the supporting information file presents SEM images illustrating the structural changes in the Mn-BDD_{AN} sample before and after undergoing 50000 charge-discharge cycles. Typically, during the ion intercalation/deintercalation process, the volume of the electrode material undergoes expansion and subsequent contraction. This phenomenon can cause irreversible damage to the structure of active materials and a reduction in the availability of active energy storage sites, causing a significant decline in capacitance retention throughout the cyclic process.[63] Remarkably, in our specific case, the Mn-BDD_{AN} sample maintained its 3D interconnected granular structure with minimal fragmentation and the absence of falling debris after the charge-discharge cycles. This preservation of structure can be attributed to the amorphous nature of the active MnO_2 sites, which are less susceptible to mechanical stress and thus contribute to the overall structural stability of the electrode.[64] Nonetheless, a noticeable change in surface porosity is evident, with a reduction in surface porosity becoming apparent after 50000 charge-discharge cycles. This reduction in surface porosity results in a decrease in the accessible surface area for the electrolyte, leading to a gradual decline in capacitance retention throughout the cyclic process (82% capacitance retention after 88000 charge/discharge cycle).

Assessing the longevity of a supercapacitor, the extended charging and discharging cycles become a crucial parameter that demands careful consideration. In practical industrial applications, there is a need for an EC capacitor with prolonged durability and robust stability. The hierarchy of cyclic stability, in accordance with the energy storage mechanism, is as follows: electric double-layer capacitors (EDLC) > intercalation type supercapacitors > pseudocapacitance.[65] Surprisingly, despite featuring an intercalation pseudocapacitive component (amorphous MnO_2) on the BDD surface, our electrode material demonstrates remarkable stability over extended cyclic life. Our device offers a

dual benefit: the pseudocapacitive element contributes to achieving a high specific capacitance, while the ultra-stable EDLC component derived from the diamond lattice ensures an exceptionally long lifespan for supercapacitor devices. Another advantage of utilizing amorphous MnO_2 with a short-range crystalline structure is its preference over crystalline MnO_2.[64] Hence, the ion implantation method proves to be an efficient approach for fabricating diamond-based supercapacitors that exhibit both a high specific capacitance and exceptional cyclic stability.

Furthermore, the current approach is also applicable for the large-scale production of active materials for supercapacitors. To perform Mn ion implantation on BDD films, the samples were attached to a 4-inch wafer, and the Mn ion beam was operated with a beam current in the range of several microamperes. This illustrates the viability of the ion implantation technique for large-scale manufacturing. Therefore, according to our perspective and belief, ion implantation approach indeed a feasible approach for the larger-scale preparation of active materials for supercapacitors.

The excellent SC performance of Mn-BDD_{AN} in aqueous, redox species containing aqueous and solid-state electrolytes is due to the synergistic combination of defect induced porous network of Mn-BDD_{AN}, outstanding EC stability BDD which contributed mainly to the EDLC part and an additional pseudocapacitive Faradaic component associated with MnO_2 phase and surface oxygen functional groups. During the implantation process Mn-ion severely damages the diamond surface (as can be seen in Figure 1) and interestingly Mn ion catalyzes the formation of graphitic carbon and MnO_2 phase during the annealing process. By increasing the hydrophilicity and creating a more accessible surface area for the electrolyte, the induced oxygen groups favorably introduce more capacitance.[14] The charge storage mechanism in the presence of MnO_2 can be written according to the previously published report,[66]

$$\left(MnO_2\right)_{surface} + C^+ + e^- \Leftrightarrow MnOOC \quad (2)$$

where C represents the C^+ represents an alkali metal cation (H^+, Na^+) in the electrolyte. Here Mn ion stored charges via rapid redox reaction and changed its oxidation states between Mn^{3+} and Mn^{4+}. In addition to these MnO_2 stores charges in the form of EDLS as well.[66]

It is known that amorphous MnO_2 with short-range crystalline order is favored over crystalline MnO_2, because the disordered structures are less susceptible to mechanical stress during ion intercalation-deintercalation processes resulting in fast ion diffusion, and higher structural stability, during long charge-discharge cycles.[19,64,67,68] The excellent EC stability of sp^3 carbons (diamond phase) in a wide range of electrolytes combined with disordered amorphous MnO_2 granular particles provides the ultra-long lifetime of SC devices (> 88 000 cycles with only 18% loss of capacitance).

Hence the EC SC output of the Mn-BDD_{AN} is attributed to the reconstruction of the film surface (granular grain) resulting in a high specific surface area with easy access to the electrolyte ions due to induced oxygen groups along with additional pseudocapacitance due to MnO_2 which facilitates the charge transfer kinetics; while the ultra-high cyclic stability is facilitated by the diamond lattice combined with amorphous MnO_2.[69,70]

3. Conclusion

In summary, granular Mn-BDD_{AN} surfaces were created by high dose Mn ion implantation and post-annealing at 750 °C, making them suitable candidates for EC SC application. The transformation of pure diamond to diamond/graphite mixed phase by controlled ion bombardment and annealing treatment is reported here. The finding regarding the localization of Mn atoms and MnO_2 phase in the diamond lattice responsible for the Faradaic component is also proposed. The Mn-BDD_{AN} electrode showed high cyclic stability (≈100% retention after 10 000 cycles in aqueous solution and ≈80% retention after 88 000 cycles in polymer gel electrolyte) without using any additional current collector or organic binder which is an essential component of any commercial SC devices. The suitable granular structure supported by the dual component of the sp^3 phase surrounded by the sp^2 phase with an additional pseudocapacitive MnO_2 component builds physicochemical dynamics for a smooth flow of charge at the electrode-electrolyte interface. Therefore, in future energy storage systems, this study paves the way for the controlled preparation of transition metal-carbon-based SC electrode material.

Supporting Information

Supporting Information is available from the Wiley Online Library or from the author.

Acknowledgements

S.D. and S.K. contributed equally to this work. This research work was supported by the Polish National Agency for Academic Exchange (NAWA, under the Ulam Programme (PPN/ULM/2020/1/00282/DEC/1). R.B. acknowledges the from the National Science Centre, Poland under OPUS call in the Weave programme (Project number: 2021/43/I/ST7/03205). D. S. and B. Y. acknowledge the financial support from the National Natural Science Foundation of China (Grants No. 52172056). N. Y. thanks the financial support from the Deutsche Forschungsgemeinschaft (DFG, German Research Foundation) under the project of 457444676.

Conflict of Interest

The authors declare no conflict of interest.

Data Availability Statement

The data that support the findings of this study are available from the corresponding author upon reasonable request.

Keywords

boron doped diamond, capacitance retention, granular grains, Mn ion implantation, pseudocapactors, redox electrolytes

Received: July 24, 2023
Revised: October 24, 2023
Published online: November 20, 2023

[1] K. Siuzdak, R. Bogdanowicz, *Energy Technol.* **2018**, *6*, 223.
[2] L. L.i Zhang, X. S. Zhao, *Chem. Soc. Rev.* **2009**, *38*, 2520.
[3] J. R. Miller, P. Simon, *Science (80-.).* **2008**, *321*, 651.
[4] E. Frackowiak, F. Béguin, *Carbon N. Y.* **2001**, *39*, 937.
[5] P. Simon, Y. Gogotsi, *Nat. Mater.* **2008**, *7*, 845.
[6] G. Wang, L. Zhang, J. Zhang, *Chem. Soc. Rev.* **2012**, *41*, 797.
[7] D. Banerjee, K. J. Sankaran, S. Deshmukh, M. Ficek, C.-J. Yeh, J. Ryl, I.-N. Lin, R. Bogdanowicz, A. Kanjilal, K. Haenen, S. Sinha Roy, *Nanoscale* **2020**, *12*, 10117.
[8] K. Honda, T. N. Rao, D. A. Tryk, A. Fujishima, M. Watanabe, K. Yasui, H. Masuda, *J. Electrochem. Soc.* **2000**, *147*, 659.
[9] M. Yoshimura, K. Honda, R. Uchikado, T. Kondo, T. N. Rao, D. A. Tryk, A. Fujishima, Y. Sakamoto, K. Yasui, H. Masuda, *Diam. Relat. Mater.* **2001**, *10*, 620.
[10] K. Honda, T. N. Rao, D. A. Tryk, A. Fujishima, M. Watanabe, K. Yasui, H. Masuda, *J. Electrochem. Soc.* **2001**, *148*, A668.
[11] S. Yu, N. Yang, H. Zhuang, J. Meyer, S. Mandal, O. A. Williams, I. Lilge, H. Schönherr, X. Jiang, *J. Phys. Chem. C* **2015**, *119*, 18918.
[12] J. Zhang, Z.-Y. Zhao, Z.-Q. Zhang, J.-X. Pei, X. Yu, Y. Coffinier, S. Szunerits, R. Boukherroub, C.-W. Yang, *Electrochim. Acta* **2022**, *421*, 140500.
[13] Z. Zhai, N. Huang, X. Jiang, *Curr. Opin. Electrochem.* **2022**, *32*, 100884.
[14] S. Deshmukh, P. Jakobczyk, M. Ficek, J. Ryl, D. Geng, R. Bogdanowicz, *Adv. Funct. Mater.* **2022**, 2206097.
[15] N. Yang, S. Yu, J. V. Macpherson, Y. Einaga, H. Zhao, G. Zhao, G. M. Swain, X. Jiang, *Chem. Soc. Rev.* **2019**, *48*, 157.
[16] W. Wei, X. Cui, W. Chen, D. G. Ivey, *Chem. Soc. Rev.* **2011**, *40*, 1697.
[17] W. Yan, T. Ayvazian, J. Kim, Y. Liu, K. C. Donavan, W. Xing, Y. Yang, J. C. Hemminger, R. M. Penner, *ACS Nano* **2011**, *5*, 8275.
[18] M. Toupin, T. Brousse, D. Bélanger, *Chem. Mater.* **2004**, *16*, 3184.
[19] S. W. Lee, J. Kim, S. Chen, P. T. Hammond, Y. Shao-Horn, *ACS Nano* **2010**, *4*, 3889.
[20] J. Zhang, X. Zhao, Z. Huang, T. Xu, Q. Zhang, *Carbon N. Y.* **2016**, *107*, 844.
[21] M. Yao, X. Zhao, L. Jin, F. Zhao, J. Zhang, J. Dong, Q. Zhang, *Chem. Eng. J.* **2017**, *322*, 582.
[22] Y. Hou, Y. Cheng, T. Hobson, J. Liu, *Nano Lett.* **2010**, *10*, 2727.
[23] V. S. Drumm, A. D. C. Alves, B. A. Fairchild, K. Ganesan, J. C. Mccallum, D. N. Jamieson, S. Prawer, S. Rubanov, R. Kalish, L. C. Feldman, *Appl. Phys. Lett.* **2011**, *98*, 231904.
[24] S. Kunuku, C.-H. Chen, P.-Y. Hsieh, B.-R. Lin, N.-H. Tai, H. Niu, *Appl. Phys. Lett.* **2019**, *114*, 131601.
[25] M. Rycewicz, M. Ficek, K. Gajewski, S. Kunuku, J. Karczewski, T. Gotszalk, I. Wlasny, A. Wysmolek, R. Bogdanowicz, *Carbon N. Y.* **2021**, *173*, 832.
[26] G. De Cesare, S. Salvatori, R. Vincenzoni, P. Ascarelli, E. Cappelli, F. Pinzari, F. Galluzzi, *Diam. Relat. Mater.* **1995**, *4*, 628.
[27] C. P. Kealey, T. M. Klapötke, D. W. Mccomb, M. I. Robertson, J. M. Winfield, *J. Mater. Chem.* **2001**, *11*, 879.
[28] M. Niklaus, S. Rosset, P. Dubois, H. R. Shea, *MRS Online Proc. Libr.* **2009**, *1188*, 1109.
[29] A. Datta, Y.-R. Wu, Y. L. Wang, *Phys. Rev. B* **2001**, *63*, 125407.
[30] X. L. Peng, Z. H. Barber, T. W. Clyne, *Surf. Coatings Technol.* **2001**, *138*, 23.
[31] O. S. Elsherif, K. D. Vernon-Parry, J. H. Evans-Freeman, P. W. May, *Semicond. Sci. Technol.* **2012**, *27*, 065019.
[32] S. Deshmukh, K. J. Sankaran, D. Banerjee, C.-J. Yeh, K.-C. Leou, D. M. Phase, M. Gupta, I.-N. Lin, K. Haenen, S. S. Roy, P. R. Waghmare, *J. Mater. Chem. A* **2019**, *7*, 19026.
[33] M. Bernard, C. Baron, A. Deneuville, *Diam. Relat. Mater.* **2004**, *13*, 896.
[34] Y. G. Wang, S. P. Lau, B. K. Tay, X. H. Zhang, *J. Appl. Phys.* **2002**, *92*, 7253.
[35] L. Ravagnan, F. Siviero, C. Lenardi, P. Piseri, E. Barborini, P. Milani, C. S. Casari, A. Li Bassi, C. E. Bottani, *Phys. Rev. Lett.* **2002**, *89*, 285506.
[36] K. J. Sankaran, H. C. Chen, B. Sundaravel, C. Y. Lee, N. H. Tai, I. N. Lin, *Appl. Phys. Lett.* **2013**, *102*, 61604.
[37] K. J. Sankaran, K. Srinivasu, C. J. Yeh, J. P. Thomas, S. Drijkoningen, P. Pobedinskas, B. Sundaravel, K. C. Leou, K. T. Leung, M. K. Van Bael, M. Schreck, I. N. Lin, K. Haenen, *Appl. Phys. Lett.* **2017**, *110*, 261602.
[38] J. Filik, J. N. Harvey, N. L. Allan, P. W. May, J. E. P. Dahl, S. Liu, R. M. K. Carlson, *Phys. Rev. B* **2006**, *74*, 35423.
[39] E. L. H. Thomas, L. Ginés, S. Mandal, G. M. Klemencic, O. A. Williams, *AIP Adv.* **2018**, *8*, 35325.
[40] A. C. Ferrari, J. Robertson, *Phys. Rev. B* **2000**, *61*, 14095.
[41] R. Issaoui, A. Tallaire, A. Mrad, L. William, F. Bénédic, M.-A. Pinault-Thaury, J. Achard, *Phys. Status Solidi.* **2019**, *216*, 1900581.
[42] S. Birgisson, D. Saha, B. B. Iversen, *Cryst. Growth Des.* **2018**, *18*, 827.
[43] X. Liu, X. Jia, Z. Zhang, M. Zhao, W. Guo, G. Huang, H.-A. Ma, *Cryst. Growth Des.* **2011**, *11*, 1006.
[44] J. Shirafuji, Y. Sakamoto, A. Furukawa, H. Shigeta, T. Sugino, *Diam. Relat. Mater.* **1995**, *4*, 984.
[45] S. Ghodbane, D. Ballutaud, F. Omnès, C. Agnès, *Diam. Relat. Mater.* **2010**, *19*, 630.
[46] A. F. Azevedo, F. A. Souza, P. Hammer, M. R. Baldan, N. G. Ferreira, *J. Nanoparticle Res.* **2011**, *13*, 6133.
[47] H. Ma, C. Li, M. Zhang, J.-D. Hong, G. Shi, *J. Mater. Chem. A* **2017**, *5*, 17040.
[48] L. Torrisi, L. Silipigni, M. Cutroneo, A. Torrisi, *Vacuum* **2020**, *173*, 109175.
[49] A. Zhang, R. Zhao, L. Hu, R. Yang, S. Yao, S. Wang, Z. Yang, Y.-M. Yan, *Adv. Energy Mater.* **2021**, *11*, 2101412.
[50] Y. Ma, R. Wang, H. Wang, J. Key, S. Ji, *J. Power Sources* **2015**, *280*, 526.
[51] H. Xia, J. Feng, H. Wang, M. O. Lai, L. Lu, *J. Power Sources* **2010**, *195*, 4410.
[52] Y. Li, D. X. Luong, J. Zhang, Y. R. Tarkunde, C. Kittrell, F. Sargunaraj, Y. Ji, C. J. Arnusch, J. M. Tour, *Adv. Mater.* **2017**, *29*, 1700496.
[53] S. Deshmukh, D. Banerjee, J. S. Marin Quintero, S. J. Fishlock, J. Mclaughlin, P. R. Waghmare, S. S. Roy, *Carbon N. Y.* **2021**, *182*, 605.
[54] J. M. Soler, E. Artacho, J. D. Gale, A. García, J. Junquera, P. Ordejón, D. Sánchez-Portal, *J. Phys. Condens. Matter* **2002**, *14*, 2745.
[55] M. J. Van Setten, M. Giantomassi, E. Bousquet, M. J. Verstraete, D. R. Hamann, X. Gonze, G.-M. Rignanese, *Comput. Phys. Commun.* **2018**, *226*, 39.
[56] M. Sobaszek, M. Brzhezinskaya, A. Olejnik, V. Mortet, M. Alam, M. Sawczak, M. Ficek, M. Gazda, Z. Weiss, R. Bogdanowicz, *Small* **2023**, *19*, 2208265.
[57] V. Mortet, I. Gregora, A. Taylor, N. Lambert, P. Ashcheulov, Z. Gedeonova, P. Hubik, *Carbon N. Y.* **2020**, *168*, 319.
[58] M. Yuan, F. Luo, Y. Rao, J. Yu, Z. Wang, H. Li, X. Chen, *Carbon N. Y.* **2021**, *183*, 128.
[59] M. Yu, Y. Zeng, Y. Han, X. Cheng, W. Zhao, C. Liang, Y. Tong, H. Tang, X. Lu, *Adv. Funct. Mater.* **2015**, *25*, 3534.
[60] A. Huang, M. F. El-Kady, X. Chang, M. Anderson, C.-W. Lin, C. L. Turner, R. B. Kaner, *Adv. Energy Mater.* **2021**, *11*, 2100768.
[61] Z. Futera, T. Watanabe, Y. Einaga, Y. Tateyama, *J. Phys. Chem. C* **2014**, *118*, 22040.
[62] M. Cloutier, C. Harnagea, P. Hale, O. Seddiki, F. Rosei, D. Mantovani, *Diam. Relat. Mater.* **2014**, *48*, 65.
[63] Y. Zhang, L. Wang, H. Xu, J. Cao, D. Chen, W. Han, *Adv. Funct. Mater.* **2020**, *30*, 1909372.
[64] P. Shi, L. Li, L. Hua, Q. Qian, P. Wang, J. Zhou, G. Sun, W. Huang, *ACS Nano* **2017**, *11*, 444.
[65] Q. Wu, T. He, Y. Zhang, J. Zhang, Z. Wang, Y. Liu, L. Zhao, Y. Wu, F. Ran, *J. Mater. Chem. A* **2021**, *9*, 24094.

[66] Q.-Z. Zhang, D. Zhang, Z.-C. Miao, X.-L. Zhang, S.-L. Chou, *Small* **2018**, *14*, 1702883.
[67] J. Zhi, O. Reiser, F. Huang, *ACS Appl. Mater. Interfaces* **2016**, *8*, 8452.
[68] M. Huang, F. Li, F. Dong, Y. X. Zhang, L. L.i Zhang, *J. Mater. Chem. A* **2015**, *3*, 21380.
[69] J. Xu, N. Yang, S. Heuser, S. Yu, A. Schulte, H. Schönherr, X. Jiang, *Adv. Energy Mater.* **2019**, *9*, 1803623.
[70] D. Banerjee, K. J. Sankaran, S. Deshmukh, C.-J. Yeh, M. Gupta, I.-N. Lin, K. Haenen, A. Kanjilal, S. Sinha Roy, *Electrochim. Acta* **2021**, *397*, 139267.